Tropopause folds over the Tibetan Plateau and their impact on water vapor in the upper troposphere-lower stratosphere

Yongpeng Zhang (ypzhang20@lzu.edu.cn)
LZU: Lanzhou University https://orcid.org/0000-0001-7901-4031
Qian Huang
LZU: Lanzhou University
Kun Guo
LZU: Lanzhou University
Mengyuan Wang
LZU: Lanzhou University
Huiren Liao
LZU: Lanzhou University
Yan Chou
LZU: Lanzhou University
Xin He
LZU: Lanzhou University

Research Article

Keywords: tropopause folds, 3D labeling method, UTLS, water vapor, Tibetan Plateau

Posted Date: April 25th, 2023

DOI: https://doi.org/10.21203/rs.3.rs-2829680/v1

Abstract

As one of the most important greenhouse gases, water vapor in the upper troposphere and lower stratosphere (UTLS) has a significant impact on the global earth-atmosphere system. The Tibetan Plateau (TP) is an important high terrain which exerts a profound impact on the change of weather and climate, and mass exchange. Tropopause folds occur frequently over the TP due to the impact of the subtropical westerly jet, which affects water vapor transport between the stratosphere and the troposphere. In this paper, the spatial and temporal distribution characteristics of tropopause folds over the TP are examined by applying an improved three-dimensional (3D) labeling algorithm to the ERA5 reanalysis data (1979 to 2019). The effects of different fold depths in various regions over the TP on the variations of UTLS water vapor are further studied. The results of a case study (25 February 2008) suggest that there is a good continuity in identification of the fold depth for the same fold event using the improved 3D labeling algorithm. The fold depth and height are consistent with the results of radiosonde data and ERA5 reanalysis data. The fold frequency over the TP shows an increasing trend in the last 41 years, with slightly lower frequency of medium folds than that of shallow folds, and lowest frequency of deep folds. There is increasing water vapor in the UTLS over the TP due to tropopause folds. The results indicate that tropopause folds enhance the horizontal divergence of water vapor in the UTLS and increase the vertical water vapor flux in the UTLS region. The folding over the plateau leads to increased moisture in the UTLS. It is argued that vertical velocity anomalies in the vicinity of the fold and subgrid perturbations have a significant impact on the increase of UTLS water vapor over the TP. The results of this work provide a scientific basis for a better understanding of the stratosphere-troposphere exchanges due to tropopause folds over the TP.

1 Introduction

There are significant differences in the dynamic and chemical characteristics of the troposphere and stratosphere, with abundant water vapor and strong vertical mixing in the troposphere, while the stratosphere is relatively dry and stable. The tropopause is not only a physical boundary connecting the troposphere and stratosphere (Pan and Munchak 2011; Pan et al. 2018), but also a transition region between the troposphere and stratosphere. The upper troposphere and lower stratosphere (UTLS) is a coupled layer between the troposphere and the stratosphere, in which variations in the distribution and concentration of radiologically active gases (water vapor, ozone, carbon dioxide, methane, nitrous oxide, etc.) lead to changes in temperature and radiative forcing (Ramaswamy and Bowen 1994; Zeng et al. 2010; Checa-Garcia et al. 2018; Xia et al. 2018; Ruiz and Prather 2022; Daskalakis et al. 2022), thus affect climate change (Solomon et al. 2007). Stratosphere-troposphere exchange (STE) across the tropopause is an important bidirectional process affecting the distribution of material in the UTLS (Holton 1990; Holton et al. 1995). The STE is associated with atmospheric processes at different scales (Gettelman et al. 2011), such as residual circulation (Holton 1990; Fueglistaler et al. 2009; Boothe and Homeyer 2017), cut-off low (Ebel et al. 1991; Sprenger et al. 2007), extratropical cyclone (Jaeglé et al. 2017), tropopause fold (Ebel et al. 1991; Škerlak et al. 2014; Söder et al. 2021), gravity wave (Fritts 1984; Fritts and

Alexander 2003; Hoffmann et al. 2013; Heller et al. 2017), convection (Tang et al. 2011; Sang et al. 2018; Phoenix and Homeyer 2021) and turbulence (Söder et al. 2021; Dörnbrack et al. 2022). The tropopause fold is an important mechanism affecting the STE, not only accompanied by upper-level frontogenesis, but also through effective mixing (Pan et al. 2004, 2007a, b). Tropopause folds are reported to contribute up to 50%-70% of the cross-tropopause exchanges in the subtropics (Sprenger et al. 2003).

About 75% of atmospheric water vapor is concentrated in the lower troposphere. Although less water vapor in the UTLS region, it is an important greenhouse gas (Held and Soden 2000; Solomon et al. 2010; Dessler et al. 2013). It also has significant effects on global climate changes by affecting radiative forcing processes, altering the energy balance of the earth-atmosphere system and the release of latent heat of condensation (Forster and Shine 2002; Zhang et al. 2004; Schneider et al. 2010; Riese et al. 2012).

The Tibetan Plateau (TP) has important thermal and dynamic effects on the Asian monsoon system, atmospheric circulation and weather and climate (Yanai and Wu 2006; Wu et al. 2007; Son et al. 2019, 2020; Babaei et al. 2021; Ren et al. 2021; Yang et al. 2022). Processes of surface evaporation, precipitation, and water vapor transport over the TP play important roles on the water cycle (Fu et al. 2006; Xu et al. 2008, 2014; Feng and Zhou 2012). Škerlak et al. (2014) revealed that the Tibetan Plateau is a global hotspot for deep STE, primarily associated with stratospheric intrusion into the troposphere. Multiple tropopauses were first detected by radiosonde temperature profiles in 2008, and were associated with tropopause folds near the subtropical westerly jet (Chen et al. 2010). It was also reported that turbulence at the top of the mixed layer can rise to the upper troposphere over the TP in winter (Chen et al. 2013, 2016). The interaction between tropopause folds and the deep boundary layer causes the ozone-rich air from the stratosphere to mix down to the near surface (500–550 hPa) over the TP (Chou et al. 2023). Moreover, it was found that tropopause folds were generated due to intensified Asian summer monsoon circulation and resulting intensified subsidence (Wu et al. 2018). These studies allow for a better understanding of the tropopause structure, the stratospheric air intrusion processes over the TP and the importance of the STE, but little is known about the quantitative spatial-temporal distribution of tropopause folds over the TP and their contribution to water vapor transport in UTLS.

Sprenger et al. (2003) proposed a three-dimensional (3D) labeling algorithm to identify folds of dynamical tropopause by distinguishing between positive potential vorticity (PV) anomalies (amplitude > 2 PVU) caused by stratospheric intrusions (> 2 PVU) and by diabatic and frictional processes in the troposphere. Based on this, Škerlak et al. (2015) further refined the 3D labeling algorithm to correctly identify stratospheric and tropospheric air in complex situations, and developed a Lagrangian filter to ensure that only tropopause folds, not diabetically or frictionally produced PV, are detected.

Based on the study of (Škerlak et al. 2015), the criteria for defining the vertical extent of folds (the fold depth) are improved in the 3D labeling algorithm. The improved 3D labeling algorithm is applied to the ERA5 reanalysis data for the period from 1979 to 2019 to investigate the climatology of tropopause folds over the TP and the effect on water vapor in the UTLS. In section 2, the data used, the improved 3D labeling algorithm and the calculation of the fold frequency are described. The identifications of a fold

event using the 3D labeling algorithm, the spatial and temporal of tropopause fold distributions over the TP are presented in section 3. The effects of the folds on water vapor in UTLS are further investigated in section 4. Finally, we present the conclusions in section 5.

2 Data And Methods

2.1 Data

The data used in this paper are the ERA5 global reanalysis datasets from 1 January 1979 to 31 December 2019 from the European Centre for Medium-Range Weather Forecasts (ECMWF). These datasets are available at a spatial resolution of 0.25° × 0.25° and a temporal resolution of 1h with 37 pressure levels from 1000 hPa to 1 hPa. The data used includes potential vorticity, specific humidity, temperature, horizontal wind speeds, vertical velocity, and surface pressure. To evaluate the identification of the fold depth using the 3D labeling algorithm before and after the improvement, data on 25 February 2008 from the ERA5 data set T639 (HRES) was used.

The Atmospheric Infrared Sounder (AIRS) was launched on the Aqua research satellite, a major component of NASA's Earth Observing System, in May 2002. The specific humidity of the AIRS from 2002 to 2019, which is the standard retrieval monthly averages with a spatial resolution of 1° × 1°, was compared with that from the ERA5 reanalysis.

2.2 Methods

2.2.1 Definition of the tropopause

The tropopause is defined in various ways, among which the thermal and dynamical definitions are common. The thermal tropopause was defined by the World Meteorological Organization (WMO) in 1957, based on the lapse rate of temperature (WMO, 1957). The tropopause at mid-latitudes is discontinuous and presents multiple tropopauses in the vicinity of the polar jet, although the thermal tropopause is easy to be determined from a radiosonde profile. Given that the vertical temperature gradient is not a conservative quantity, the definition of the thermal tropopause does not accurately describe air mass characteristics of the stratosphere and troposphere (Wilcox et al., 2012). The dynamical tropopause is defined in terms of potential vorticity, taking into account the effects of atmospheric stability, atmospheric circulation and air density (Hoskins et al. 1985; Holton et al. 1995). In the northern hemisphere, the dynamical tropopause is defined by PV values in the range of 1–4 PVU (1 PVU = 1×10^{-6} $K\cdot m^2\cdot kg^{-1}\cdot s^{-1}$) (Kunz et al. 2011). A definition of the blended tropopause combines the characteristics of both dynamical and thermal tropopause (Wilcox et al. 2012; Mateus et al. 2022). In this paper, the dynamical tropopause is defined as the lower height of the isosurface of PV at 2 PVU and isentropic surface at θ = 380 K (Hoskins et al. 1985; Holton et al. 1995; Stohl et al. 2003; Sprenger et al. 2003; Škerlak et al. 2015).

2.2.2 Improved 3D labeling algorithm and Lagrangian filter

The 3D labeling algorithm refined by Škerlak et al. (2015) has been used in many studies to detect tropopause folds (Akritidis et al. 2016, 2019, 2021; Breeden et al. 2021; Dafka et al. 2021). In this work, we further improve the determination of the fold depth based on the algorithm from Škerlak et al. (2015), as shown in Fig. 1. Following the 3D labeling algorithm of Škerlak et al. (2015), the air in the troposphere and stratosphere is first classified into five categories according to the isosurface of PV at 2 PVU (or θ = 380 K) and specific humidity (0.1 $g \cdot kg^{-1}$) (as shown in Fig. 1a). The categories are: tropospheric air (label 1), stratospheric air (label 2), isolated stratospheric air or diabetically generated cyclonic PV anomalies (stratospheric cutoffs, label 3), isolated tropospheric air (tropospheric cutoffs, label 4) and frictionally generated PV anomalies (label 5). If multiple tropopauses are determined for grid locations in the labeled field (i.e., there are multiple crossings of the interface between stratosphere and troposphere), an occurrence of fold is tentatively determined at that grid. The connectedness analysis is then used to detect whether folds at various grids are spatially connected. To confirm that the identification of the fold is not associated with PV anomalies produced by the diabatic processes (diabetically heating effects of clouds) and friction, 24 h backward trajectories are performed for the grids inside a tropopause fold detected by the 3D labeling algorithm. The grid points detected as tropopause folds are discarded if label 3, 4 or 5 is encountered along the trajectories, because PV anomalies are associated with diabatic or frictional processes and not with a true stratospheric fold. In addition, the pressure difference ΔP between the grid points accessing the dynamical tropopause (Fig. 1a) is applied to classify the tropopause fold (Sprenger et al. 2003).

As the pressure difference between grids in the vertical column is used to identify the vertical extent of the fold, there are various fold depths classified in a fold event. However, the pressures and physical properties of the air mass of grid points are not identical at the same isosurface within the fold even if there are grid points with the same pressure difference. Therefore, the maximum pressure difference of the interconnected grid points at 2 PVU surfaces within the fold is calculated, and finally used to indicate the vertical extent of the fold (as shown by the solid brown line in Fig. 1b). In this paper, the classification of the tropopause fold given by (Tyrlis et al. 2014) is adopted, i.e. folds with 50 ≤ ΔP < 200 hPa, 200 ≤ ΔP < 350 hPa and ΔP ≥ 350 hPa are cataloged as shallow folds, medium folds, and deep folds, respectively.

2.2.3 Fold frequency

The improved 3D labeling algorithm is used to evaluate the occurrence of tropopause folds and to classify the fold depth over the TP for the 41-year time period from January 1, 1979 to December 31, 2019. The fold frequency at each grid point, f_{TF}, is defined as

$$f_{TF}\left(lat, lon\right) = \frac{\sum_{i=1}^{i=N} F_i(lat,lon)}{N}, \#\left(1.\right)$$

where N is time, lat and lon are latitude and longitude, respectively, and Fi is the fold occurrence count, which is determined by

$$F_i\left(lat, lon\right) = \begin{cases} 1, C_{fd} \leq \Delta P_i \\ 0, others \end{cases}, \#\left(2\right)$$

where ΔP_i is the pressure difference, C_{fd} is the threshold of the pressure difference for the classification of tropopause folds. Following Tyrlis et al. (2014), fold structures with ΔP_i less than 50 hPa are discarded, and the threshold C_{fd} of 50 hPa is used to define the total fold frequency. The thresholds C_{fd} for the classification of tropopause folds are defined in section 2.2.2.

3 Distribution Of Folds

3.1 Algorithm verification

To verify the algorithm, a tropopause fold event identified by 3D labeling algorithm before (Figure. 2a and 2c) and after (Figure. 2b and 2d) improvement are compared at 11 UTC on 25 February 2008. As can be seen in Fig. 2, there is a good agreement in the identification of fold location and depth, but differences in fold classification. Figure. 2a and 2c show that two fold categories (shallow and medium folds) are identified at 11 UTC by the algorithm before improvement, but only a medium fold is determined after improvement (Figure. 2b and 2d). Although the depth of the stratospheric intrusion varies in different regions for a fold event (ΔP varies), the synoptic weather system that triggers a fold is unique. If a fold event is categorized to different depths at the same time, it does not correspond well to the synoptic system that initiates a tropopause fold (e.g., upper tropospheric frontogenesis or jet stream). Therefore, the distribution of folds is hereafter determined by the improved 3D labeling algorithm in this work.

The distribution of potential temperature, zonal wind speed, potential vorticity (from the ERA5 reanalysis data), fold depth (using 3D labeling algorithm) and the radiosonde profiles at Gerze (32.17°N, 84.03°E, with the elevation of 4415 m) for the same case study shown in Fig. 2 are further presented in Fig. 3. The radiosonde data is obtained from the first stage (IPO1) of the Sino-Japanese Center for Cooperation on Meteorological Disasters research project (JICA) at Gerze. Figure 3a shows that the tropopause fold develops in a high-level frontal zone along the subtropical jet stream on the southern TP. It grows to a deep fold at 01 UTC on 26 February with the tropopause dipping down to 378 hPa (Figure S1, in the supplement). Specific humidity and temperature decrease with the altitude near the tropopause at Gerze (Fig. 3b). There is an inversion between the 340 hPa and 280 hPa layers, probably caused by the stratospheric intrusion. Another tropopause can be seen at about 100 hPa, confirming the frequent occurrence of multiple tropopause events over the TP (Pan et al. 2007a; Chen et al. 2011). The radiosonde wind profiles show (Fig. 3c) that the jet stream occurs at 300 – 180 hPa, which is consistent with the location and intensity of the jet stream analyzed using the ERA5 reanalysis data. The green shading in Fig. 3a indicates that the depth of the stratospheric intrusion identified by the improved 3D labeling algorithm penetrates down to 375 hPa, which is generally consistent with the inversion at about 340 hPa from the radiosonde profile. Thus, the isosurface of PV at 2 PVU (or θ = 380 K)determined using this algorithm can describe the tropopause over the TP. The fold area (green shading) in Fig. 3a is detached, which means that the tropospheric air mass in the discontinuous region does not fulfill the 2

PVU criteria to be labeled the stratospheric intruding air. Further analysis indicates that the fold at the lower latitude (30°N) is connected to the adjacent folds (Figure S2), therefore, the fold in Fig. 3a is considered to be a fold event. PV anomalies occurring near the surface and in the lower troposphere (e.g., near 28°N in Fig. 3a) are distinguished from those inside the fold, which indicates that the algorithm is able to accurately identify the fold event and its spatial distribution using high-resolution data.

3.2 Tropopause folds distribution

3.2.1 Seasonal distribution

There is a lack of quantitative studies of the temporal and spatial distribution of tropopause folds over the TP, although considerable statistical analyzes of fold frequencies have been performed at global (Sprenger et al. 2003; Škerlak et al. 2015; Akritidis et al. 2021) and regional scales (Chen et al. 2011; Akritidis et al. 2016; Wu et al. 2018; Luo et al. 2019; Dafka et al. 2021; Borhani et al. 2022). In this study, an improved 3D labeling algorithm is used to investigate the frequency of tropopause folds over the TP in different seasons from January 1, 1979 to December 31, 2019. Figure 4 shows that folds occur along the subtropical jet stream and follow the northward or southward migration of the subtropical jet stream, in agreement with previous studies ((Wu et al. 2018; Luo et al. 2019). Tropopause folds occur mainly in the southern Tibetan Plateau in winter and spring, and move westward from winter to spring. In summer, folds are distributed primarily in the northwest TP, with the highest frequencies (greater than 12%) in the Pamir region (60°E-80°E, 34°N-42°N), and a maximum frequency of about 16%. The region where summer folds occur is adjacent to frequently occurring intense convective systems over the TP (Wu et al. 2016), which is attributed to the decrease of static stability beneath the folds due to the stratospheric intrusion (Škerlak et al. 2015; Söder et al. 2021). The fold frequency is low in autumn with relatively uniform distribution within the subtropical jet stream. Overall, the fold frequencies in the south or northwest of the TP are much lower in autumn than in other seasons.

Global and regional climatology studies of tropopause folds have shown that most folds are vertically shallow (Sprenger et al. 2003; Škerlak et al. 2015; Luo et al. 2019). However, this study using an improved 3D algorithm detects significantly increased frequencies of medium folds over the TP, reaching up to 7% in summer. Seasonal cycles of three classes of tropopause folds are further investigated, and show (Figure S3 in the supplement) that the peaks in shallow frequencies occur in spring, and the minima in autumn with more even distribution within the jet stream. Medium folds are primarily distributed in the south and southeast of the TP in DJF and MAM, which corresponds well with the subtropical jet stream. In the summer months (JJA), high-medium fold frequencies are found in the northwest of the TP, but outside of the jet stream. In winter, deep folds occur mainly over the south of the Himalayas with occurrence frequency of up to about 49% of the total annual deep fold occurrence.

3.2.2 EOF analysis of fold frequencies

To further examine the interannual spatial-temporal variability of tropopause fold frequencies, the empirical orthogonal functions (EOFs) of fold frequencies over the TP for a time period from 1979 to

2019 are analyzed. The Mann-Kendall test (Kendall and Stuart, 1961) is used to detect the trend in tropopause fold frequencies. The first mode, explaining 31.1% of total variance in tropopause folds, shows (Fig. 5a) a north-south structure. The maximum correlation coefficient of 0.92 lies in the eastern part of the TP. There is an upward trend in the occurrence of tropopause folds at the 95% confidence level. The second EOF, which explains 13.2% of total variance, shows a dipolar structure (Figure S4a). The first EOF of shallow folds explaining 23% of the total variance shows a dipolar frequency variability (Fig. 5b), with an increasing trend over the TP. The second EOF of shallow folds explains 15.5% of the variance (Figure S4b). The spatial distribution of the first EOF of medium folds is characterized by a homogeneous positive value, with the maxima at the southern edge of the TP. The first EOF of medium folds explains almost half of the variance (45.7%), with a significant upward trend for the period from 1979 to 2019. The first mode accounts for about 26% of the variance of the deep fold occurrence, with no significant upward trend.

The zonally averaged maximum height of the tropopause folds is defined as the fold height in the present work, and is further used to evaluate the altitude of the stratospheric intrusion over the TP. The fold heights show (Figure S5, in the supplementary material) that the height of folds over the TP (20°N-50°N, 50°E-115°E) decreases with increasing latitude, more significantly north of 36°N, especially for deep folds. This is consistent with the results that the tropopause height decreases gradually from the equator to the poles (Wilcox et al. 2012). Overall, the fold heights are significantly larger in the southern part of the TP than in the north.

4 Effect Of Tropopause Folds On Utls Water Vapor

4.1 Water vapor flux in the UTLS

To validate the accuracy of water vapor in the ERA5 reanalysis datasets, the humidity derived from the ERA5 and the AIRS satellite observations are compared for a time period from 2002 to 2019. Due to the various spatial-temporal resolutions of the data sets used, moisture at the same grid point and the same time of both data sets are compared. Figure 6 shows that specific humidity derived from the ERA5 is in good agreement with that from the AIRS satellite observations, with R^2 = 0.98 and a slope of about 1.01. Therefore, the water vapor from ERA5 reanalysis data is used to study the effect of the tropopause fold on water vapor in the UTLS over the TP.

Atmospheric convection, the South Asian High, and atmospheric temperature play a significant role on the water vapor content of UTLS over the Tibetan Plateau and surrounding areas (Wu et al. 2015; Son et al. 2020; Ren et al. 2021). However, variations of water vapor in UTLS are initiated by tropospheric processes. Tropopause folds and their impact on the UTLS water vapor over the TP are studied in this work, which presents the dynamic transport from the stratosphere to the troposphere. Figure 7b is a comparison of the water vapor content in the UTLS (300-50hPa) over the TP (shaded area in Fig. 7a) between the situations with no fold and the various folds. The water vapor content in the UTLS is clearly seen to increase due to tropopause folds, with a greater increase in shallow and medium folds, and a

lower increase in deep folds, largely consistent with the frequency of folds over the TP. The UTLS water vapor flux on the boundaries of the TP shows that folds increase the outward transport of water vapor on the northern boundary of the TP, while reducing the transport of water vapor from the southern boundary into the TP (Fig. 7c). Meanwhile, folds weaken the water vapor transport of the westerlies, but enhance the outward transport from the eastern boundary of the TP. This indicates that stratospheric intrusion induces a significant increase in horizontal divergence over the TP (Figure S6 in the supplementary material), which leads to an increase in horizontal transport of UTLS water vapor to the outside of the TP. However, the vertical flux of water vapor in the UTLS increases due to tropopause folds, as shown in Fig. 7d. This not only compensates the reduction of water vapor in UTLS owing to the increase of horizontal divergence, but also leads to a net increase of water vapor in the UTLS over the TP (Fig. 7b).

Since the distribution of the folds over the TP is characterized by the north-south belt and the height of folds decreases sharply with height in the northern part of the TP (about 36°N), we further analyze the effect of fold locations on water vapor in the UTLS over the TP. The TP is partitioned into three regions along latitudes 44°N, 36°N and 30°N (Fig. 8a). Here the location of folds is determined by where the fold dips to its lowest point. Figure 8b shows that the water vapor content in the UTLS increases with occurrence of folds. The increase of water vapor decreases with folds moving from the northern zone I to the southern zone III over the TP. Figure 4c suggests that the highest frequency of folds in summer occurs in the northwest of the TP. Therefore, the increase in water vapor due to folds in the zone I is not only associated with abundant water vapor in summer but also with the transport of deep convection around this region (Wu et al. 2016).

4.2 Effects of secondary circulation and subgrid mixing on water vapor

The upward transport of water vapor in the UTLS of the TP increases with the occurrence of tropopause folds (Fig. 7d). It is interesting to investigate the changes in vertical circulation anomalies and water vapor anomalies around the fold. The three-dimensional vertical velocity anomalies, water vapor mixing ratio anomalies and horizontal velocity anomalies at different pressure levels corresponding to different folds over the TP are shown in Fig. 9. Note that (0°N, 0°E) corresponds to the deepest point that the folded tropopause intrudes to, which means that all folds have moved to the same location. Figure 9 shows that the occurrence of folds is also accompanied by vertical velocity anomalies (circulation anomalies). It is worth noting that it is a secondary circulation associated with the tropopause folds which is not directly related to circulation fields over East Asia. There are positive anomalies of water vapor in updrafts, and negative anomalies in downdrafts. Cyclonic anomalies appear in shallow, medium, and deep folds at 200 hPa. Since tropopause folds over the TP are generally associated with the subtropical westerly jet (Chen et al. 2011), vertical velocity anomalies in the vicinity of tropopause folds are also related to the vertical motion caused by the convergence or divergence at the jet entrance or exit. Secondary circulation anomalies and cyclonic anomalies are most significant in deep folds extending even to the TP surface (Figure S7 in the supplementary material) while higher water vapor anomalies are seen in shallow and medium folds. Figure 9 also shows that vertical velocity anomalies are most

significant in deep folds but weakest in shallow folds. This is because deep folds occur primarily in winter and spring when there is a stronger subtropical westerly jet, and corresponding stronger convergence or divergence at the jet entrance and exit. Moreover, it has been reported that the tropopause becomes folded during upper tropospheric frontogenesis (Hoskins 1982). The anomalous vertical velocity enhances the temperature gradient, thereby strengthening the frontal zone and increasing isentropic slopes. It results the transport of stratospheric dry air into the troposphere along isentropic surfaces and tropospheric water vapor into the UTLS.

It has been reported that turbulent mixing in the vicinity of tropopause folds has a significant impact on the STE (Shapiro 1980; Chen et al. 2013, 2016; Yin et al. 2017; Söder et al. 2021). The transport of water vapor caused by subgrid eddies ($\overline{w'q'}$) in the UTLS over the TP (the shaded area in Fig. 7a) for different folds are shown in Fig. 10. It shows that the subgrid perturbation increases the upward transport of water vapor and the downward transport of dry air ($\overline{w'q'} > 0$) with the occurrence of shallow and medium folds, especially significant in medium folds. The subgrid water vapor flux $\overline{w'q'}$ is negative in deep folds, maybe related to the relative dry air in winter when deep folds occur frequently. Water vapor flux $\overline{w'q'}$ is also negative when there is no fold occurrence. This indicates that small scale mixing (turbulent mixing) in the vicinity of a fold also contributes to the increase of water vapor in the UTLS of the TP, which is more significant for the vertical mixing in the vicinity of frequently occurring folds. Therefore, the increase of water vapor in the UTLS of the TP is also related to vertical circulation anomalies associated with the subtropical westerly jet and upper-level frontogenesis on one hand, and to turbulent mixing due to folds on the other hand.

5 Conclusion

This study presents the climatology of tropopause folds over the Tibetan Plateau, determined using an improved 3D labeling algorithm based on the ERA5 data set from 1979 to 2019. The spatial and temporal distribution characteristics of tropopause folds over the TP are first investigated. The effects of the tropopause fold over the TP on water vapor variations in the UTLS is then discussed. Water vapor transport mechanisms in the UTLS are explained by investigating the secondary circulation associated with the subtropical jet stream and the upper level frontogenesis as well as subgrid water vapor flux for different folds. The major conclusions of this work are as follows.

The 3D labeling algorithm improves the detection of horizontal connectedness of the different folds and modifies the identification of fold depth. The occurrence time and location of the tropopause folds determined by the 3D labeling algorithm are consistent before and after the improvement, but the improved algorithm improves the continuity in the determination of the vertical extent of folds. In a case study, the identification of fold location and fold depth are consistent with radiosonde profiles. The seasonal distribution of fold frequencies over the TP during the past 41 years is consistent with that of the subtropical jet stream, which moves poleward as the season progresses. Tropopause folds occur

primarily at the southern edge of the TP in winter and spring, and in the northwest in summer. The maximum fold frequency is found in the western edge of the TP in summer. Relatively low and even fold frequencies are found in the autumn. A north-south structure of tropopause folds over the TP is confirmed by the EOF analysis and show a significant upward trend for medium and shallow folds during 1979–2019. It is also found that the fold height over the TP decreases with increase in latitude, most significantly north of 36°N.

Water vapor comparisons in the UTLS between situations with and without tropopause folds reveal that folds increase the horizontal divergence in the UTLS, which leads to an outflow of water vapor at the northern boundary of the TP and a reduction of water vapor transport at the southern boundary. The vertical transport of water vapor in the UTLS varies significantly due to tropopause folds, with increased upward transport of shallow, medium and deep folds. Folds are accompanied by secondary circulation anomalies associated with the subtropical jet stream and frontal zone system. Anomalous updrafts transport water vapor from the troposphere to the UTLS. Meanwhile, the stratospheric dry air mixes down into the troposphere along the isentropic surface. Water vapor content increases in the UTLS with the occurrence of folds. The most significant increase of water vapor is found at the location of tropopause folds in the north of the TP (zone I), maybe related to frequent deep convection in the north-west of the TP in summer. The concentration of water vapor increases when folds occur in the TP, with a more pronounced increase in water vapor when the folds occur in the northern TP compared to the southern region. In addition, the subgrid perturbation associated with the tropopause fold also increases the transport of UTLS water vapor of the Tibetan Plateau. The results of this work provide a scientific basis for a better understanding of the stratosphere-troposphere exchanges due to tropopause folds over the TP.

Declarations

Acknowledgments

This paper is supported by National Natural Science Foundation of China (NSFC) under grant No.42175088, No. 42075060 and No.41905011. The authors thank all the participants from China and Japan for their work collecting the JICA Tibetan Plateau meteorological observations.

Data Availability

The datasets analysed during the current study are available in the ERA5 repository, https://www.ecmwf.int/en/forecasts/dataset/ecmwf-reanalysis-v5 and GES DISC repository, https://disc.gsfc.nasa.gov/datasets/AIRS2SUP_7.0/summary?keywords=_%22AIRS%22 And the improved 3D labeling algorithm program cloud be found in github repository, https://github.com/jokervTv/folding-detection.

Conflict of Interests

The authors have no conflicts of interest to declare that are relevant to the content of this article.

Author Contributions

Yongpeng Zhang performed the data analysis, prepared all figures, and wrote the manuscript. Qian Huang and Yongpeng Zhang designed the research and revised the manuscript. Xin He, Kun Guo, Mengyuan Wang, Huiren Liao and Yan Chou revised the manuscript. Data collection were performed by Xin He. All the authors discussed the results and approved the final manuscript.

References

1. Akritidis D, Pozzer A, Flemming J, et al (2021) A global climatology of tropopause folds in CAMS and MERRA-2 reanalyses. J. Geophys. Res. Atmos. 126:e2020JD034115. https://doi.org/10.1029/2020jd034115
2. Akritidis D, Pozzer A, Zanis P, et al (2016) On the role of tropopause folds in summertime tropospheric ozone over the eastern Mediterranean and the Middle East. Atmos. Chem. Phys. 16:14025–14039. https://doi.org/10.5194/acp-16-14025-2016
3. Akritidis D, Pozzer A, Zanis P (2019) On the impact of future climate change on tropopause folds and tropospheric ozone. Atmos. Chem. Phys. 19:14387–14401. https://doi.org/10.5194/acp-19-14387-2019
4. Babaei M, Alizadeh O, Irannejad P (2021) Impacts of orography on large-scale atmospheric circulation: application of a regional climate model. Clim. Dyn. 57:1973–1992. https://doi.org/10.1007/s00382-021-05790-0
5. Boothe AC, Homeyer CR (2017) Global large-scale stratosphere–troposphere exchange in modern reanalyses. Atmos. Chem. Phys. 17:5537–5559. https://doi.org/10.5194/acp-17-5537-2017
6. Borhani R, Ahmadi-Givi F, Ghader S, Mohebalhojeh AR (2022) A climatological-dynamical analysis of tropopause folds over Southwest Asia in the period of 1989–2018. Dyn. Atmos. Oceans 98:101300. https://doi.org/10.1016/j.dynatmoce.2022.101300
7. Breeden ML, Butler AH, Albers JR, et al (2021) The spring transition of the North Pacific jet and its relation to deep stratosphere-to-troposphere mass transport over western North America. Atmos. Chem. Phys. 21:2781–2794. https://doi.org/10.5194/acp-21-2781-2021
8. Checa-Garcia R, Hegglin MI, Kinnison D, et al (2018) Historical Tropospheric and Stratospheric Ozone Radiative Forcing Using the CMIP6 Database. Geophys. Res. Lett. 45:3264–3273. https://doi.org/10.1002/2017GL076770
9. Chen X, Añel JA, Su Z, et al (2013) The Deep Atmospheric Boundary Layer and Its Significance to the Stratosphere and Troposphere Exchange over the Tibetan Plateau. PLOS ONE 8:e56909. https://doi.org/10.1371/journal.pone.0056909

10. Chen X, Škerlak B, Rotach MW, et al (2016) Reasons for the Extremely High-Ranging Planetary Boundary Layer over the Western Tibetan Plateau in Winter. J. Atmos. Sci. 73:2021–2038. https://doi.org/10.1175/JAS-D-15-0148.1
11. Chen XL, Ma YM, Kelder H, et al (2011) On the behaviour of the tropopause folding events over the Tibetan Plateau. Atmos. Chem. Phys. 11:5113–5122. https://doi.org/10.5194/acp-11-5113-2011
12. Chou Y, Huang Q, Zhang Y, et al (2023) Impacts of deep boundary layer on near-surface ozone concentration over the Tibetan Plateau. Atmospheric Environ. 294:119532. https://doi.org/10.1016/j.atmosenv.2022.119532
13. Dafka S, Akritidis D, Zanis P, et al (2021) On the link between the Etesian winds, tropopause folds and tropospheric ozone over the Eastern Mediterranean during summer. Atmos. Res. 248:105161. https://doi.org/10.1016/j.atmosres.2020.105161
14. Daskalakis N, Gallardo L, Kanakidou M, et al (2022) Impact of biomass burning and stratospheric intrusions in the remote South Pacific Ocean troposphere. Atmos. Chem. Phys. 22:4075–4099. https://doi.org/10.5194/acp-22-4075-2022
15. Dessler AE, Schoeberl MR, Wang T, et al (2013) Stratospheric water vapor feedback. Proc. Natl. Acad. Sci. 110:18087–18091. https://doi.org/10.1073/pnas.1310344110
16. Dörnbrack A, Bechtold P, Schumann U (2022) High-Resolution Aircraft Observations of Turbulence and Waves in the Free Atmosphere and Comparison With Global Model Predictions. J. Geophys. Res. Atmos. 127:e2022JD036654. https://doi.org/10.1029/2022JD036654
17. Ebel A, Hass H, Jakobs HJ, et al (1991) Simulation of ozone intrusion caused by a tropopause fold and cut-off low. Atmos. Environ., Part A 25:2131–2144. https://doi.org/10.1016/0960-1686(91)90089-P
18. Feng L, Zhou T (2012) Water vapor transport for summer precipitation over the Tibetan Plateau: Multidata set analysis. J. Geophys. Res. Atmos. 117:D20114. https://doi.org/10.1029/2011JD017012
19. Forster PM de F, Shine KP (2002) Assessing the climate impact of trends in stratospheric water vapor. Geophys. Res. Lett. 29:10-1-10–4. https://doi.org/10.1029/2001GL013909
20. Fritts DC (1984) Gravity wave saturation in the middle atmosphere: A review of theory and observations. Rev. Geophys. 22:275–308. https://doi.org/10.1029/RG022i003p00275
21. Fritts DC, Alexander MJ (2003) Gravity wave dynamics and effects in the middle atmosphere. Rev. Geophys. 41:1003. https://doi.org/10.1029/2001RG000106
22. Fu R, Hu Y, Wright JS, et al (2006) Short circuit of water vapor and polluted air to the global stratosphere by convective transport over the Tibetan Plateau. Proc. Natl. Acad. Sci. 103:5664–5669. https://doi.org/10.1073/pnas.0601584103
23. Fueglistaler S, Dessler AE, Dunkerton TJ, et al (2009) Tropical tropopause layer. Rev. Geophys. 47:RG1004. https://doi.org/10.1029/2008RG000267
24. Gettelman A, Hoor P, Pan LL, et al (2011) The Extratropical Upper Troposphere and Lower Stratosphere. Rev. Geophys. 49:RG3003. https://doi.org/10.1029/2011RG000355

25. Held IM, Soden BJ (2000) Water Vapor Feedback and Global Warming. Annu. Rev. Environ. Resour. 25:441–475. https://doi.org/10.1146/annurev.energy.25.1.441
26. Heller R, Voigt C, Beaton S, et al (2017) Mountain waves modulate the water vapor distribution in the UTLS. Atmos. Chem. Phys. 17:14853–14869. https://doi.org/10.5194/acp-17-14853-2017
27. Hoffmann L, Xue X, Alexander MJ (2013) A global view of stratospheric gravity wave hotspots located with Atmospheric Infrared Sounder observations. J. Geophys. Res. Atmos. 118:416–434. https://doi.org/10.1029/2012JD018658
28. Holton JR (1990) On the Global Exchange of Mass between the Stratosphere and Troposphere. J. Atmos. Sci. 47:392–395. https://doi.org/10.1175/1520-0469(1990)047<0392:OTGEOM>2.0.CO;2
29. Holton JR, Haynes PH, McIntyre ME, et al (1995) Stratosphere-troposphere exchange. Rev. Geophys. 33:403. https://doi.org/10.1029/95RG02097
30. Hoskins BJ (1982) The Mathematical Theory of Frontogenesis. Annu. Rev. Fluid. Mech. 14:131–151. https://doi.org/10.1146/annurev.fl.14.010182.001023
31. Hoskins BJ, McIntyre ME, Robertson AW (1985) On the use and significance of isentropic potential vorticity maps. Quart. J. Roy. Meteor. Soc. 111:877–946. https://doi.org/10.1002/qj.49711147002
32. Jaeglé L, Wood R, Wargan K (2017) Multiyear Composite View of Ozone Enhancements and Stratosphere-to-Troposphere Transport in Dry Intrusions of Northern Hemisphere Extratropical Cyclones. J. Geophys. Res. Atmos. 122:13,436-13,457. https://doi.org/10.1002/2017JD027656
33. Kendall M G and Stuart A (1961) The advanced theory of statistics. Inference and relationship. 3rd Edition, Griffin, London.
34. Kunz A, Konopka P, Müller R, Pan LL (2011) Dynamical tropopause based on isentropic potential vorticity gradients. J. Geophys. Res. Atmos. 116:D01110. https://doi.org/10.1029/2010JD014343
35. Luo J, Liang W, Xu P, et al (2019) Seasonal Features and a Case Study of Tropopause Folds over the Tibetan Plateau. Adv. Meteorol. 2019:1–12. https://doi.org/10.1155/2019/4375123
36. Mateus P, Mendes VB, Pires CAL (2022) Global Empirical Models for Tropopause Height Determination. Remote Sens. 14:4303. https://doi.org/10.3390/rs14174303
37. Pan LL, Bowman KP, Shapiro M, et al (2007a) Chemical behavior of the tropopause observed during the Stratosphere-Troposphere Analyses of Regional Transport experiment. J. Geophys. Res. Atmos. 112:D18110. https://doi.org/10.1029/2007JD008645
38. Pan LL, Honomichl SB, Bui TV, et al (2018) Lapse Rate or Cold Point: The Tropical Tropopause Identified by In Situ Trace Gas Measurements. Geophys. Res. Lett. 45:10,756-10,763. https://doi.org/10.1029/2018GL079573
39. Pan LL, Munchak LA (2011) Relationship of cloud top to the tropopause and jet structure from CALIPSO data. J. Geophys. Res. 116:D12201. https://doi.org/10.1029/2010JD015462
40. Pan LL, Randel WJ, Gary BL, et al (2004) Definitions and sharpness of the extratropical tropopause: A trace gas perspective. J. Geophys. Res. Atmos. 109:D23103. https://doi.org/10.1029/2004JD004982

41. Pan LL, Wei JC, Kinnison DE, et al (2007b) A set of diagnostics for evaluating chemistry-climate models in the extratropical tropopause region. J. Geophys. Res. Atmos. 112:D09316. https://doi.org/10.1029/2006JD007792
42. Phoenix DB, Homeyer CR (2021) Simulated Impacts of Tropopause-Overshooting Convection on the Chemical Composition of the Upper Troposphere and Lower Stratosphere. J. Geophys. Res. Atmos. 126:e2021JD034568. https://doi.org/10.1029/2021JD034568
43. Ramaswamy V, Bowen MM (1994) Effect of changes in radiatively active species upon the lower stratospheric temperatures. J. Geophys. Res. Atmos. 99:18909–18921. https://doi.org/10.1029/94JD01310
44. Ren Q, Jiang X, Zhang Y, et al (2021) Effects of Suppressed Transient Eddies by the Tibetan Plateau on the East Asian Summer Monsoon. J. Climate 34:8481–8501. https://doi.org/10.1175/JCLI-D-20-0646.1
45. Riese M, Ploeger F, Rap A, et al (2012) Impact of uncertainties in atmospheric mixing on simulated UTLS composition and related radiative effects. J. Geophys. Res. Atmos. 117:D16305. https://doi.org/10.1029/2012JD017751
46. Ruiz DJ, Prather MJ (2022) From the middle stratosphere to the surface, using nitrous oxide to constrain the stratosphere–troposphere exchange of ozone. Atmos. Chem. Phys. 22:2079–2093. https://doi.org/10.5194/acp-22-2079-2022
47. Sang W, Huang Q, Tian W, et al (2018) A Large Eddy Model Study on the Effect of Overshooting Convection on Lower Stratospheric Water Vapor. J. Geophys. Res. Atmos. 123:10,023-10,036. https://doi.org/10.1029/2017JD028069
48. Schneider T, O'Gorman PA, Levine XJ (2010) Water Vapor and the Dynamics of Climate Changes. Rev. Geophys. 48:RG3001. https://doi.org/10.1029/2009RG000302
49. Shapiro MA (1980) Turbulent Mixing within Tropopause Folds as a Mechanism for the Exchange of Chemical Constituents between the Stratosphere and Troposphere. J. Atmos. Sci. 37:994–1004. https://doi.org/10.1175/1520-0469(1980)037<0994:TMWTFA>2.0.CO;2
50. Škerlak B, Sprenger M, Pfahl S, et al (2015) Tropopause folds in ERA-Interim: Global climatology and relation to extreme weather events. J. Geophys. Res. Atmos. 120:4860–4877. https://doi.org/10.1002/2014JD022787
51. Škerlak B, Sprenger M, Wernli H (2014) A global climatology of stratosphere–troposphere exchange using the ERA-Interim data set from 1979 to 2011. Atmos. Chem. Phys. 14:913–937. https://doi.org/10.5194/acp-14-913-2014
52. Söder J, Zülicke C, Gerding M, Lübken F (2021) High-Resolution Observations of Turbulence Distributions Across Tropopause Folds. J. Geophys. Res. Atmos. 126:e2020JD033857. https://doi.org/10.1029/2020JD033857
53. Solomon S, Intergovernmental Panel on Climate Change, Intergovernmental Panel on Climate Change (eds) (2007) Climate change 2007: the physical science basis: contribution of Working

Group I to the Fourth Assessment Report of the Intergovernmental Panel on Climate Change. Cambridge University Press, Cambridge; New York

54. Solomon S, Rosenlof KH, Portmann RW, et al (2010) Contributions of Stratospheric Water Vapor to Decadal Changes in the Rate of Global Warming. Science 327:1219–1223. https://doi.org/10.1126/science.1182488
55. Son J-H, Seo K-H, Wang B (2019) Dynamical Control of the Tibetan Plateau on the East Asian Summer Monsoon. Geophys. Res. Lett. 46:7672–7679. https://doi.org/10.1029/2019GL083104
56. Son J-H, Seo K-H, Wang B (2020) How Does the Tibetan Plateau Dynamically Affect Downstream Monsoon Precipitation? Geophys. Res. Lett. 47:e2020GL090543. https://doi.org/10.1029/2020GL090543
57. Sprenger M, Wernli H, Bourqui M (2007) Stratosphere–Troposphere Exchange and Its Relation to Potential Vorticity Streamers and Cutoffs near the Extratropical Tropopause. J. Atmos. Sci. 64:1587–1602. https://doi.org/10.1175/JAS3911.1
58. Sprenger, Michael Croci-Maspoli M, Wernli H (2003) Tropopause folds and cross-tropopause exchange: A global investigation based upon ECMWF analyses for the time period March 2000 to February 2001. J. Geophys. Res. Atmos. 108:8518. https://doi.org/10.1029/2002JD002587
59. Stohl A, Bonasoni P, Cristofanelli P, et al (2003) Stratosphere-troposphere exchange: A review, and what we have learned from STACCATO. J. Geophys. Res. Atmos. 108:8516. https://doi.org/10.1029/2002JD002490
60. Tang Q, Prather MJ, Hsu J (2011) Stratosphere-troposphere exchange ozone flux related to deep convection. Geophys. Res. Lett. 38:L03806. https://doi.org/10.1029/2010GL046039
61. Tyrlis E, Škerlak B, Sprenger M, et al (2014) On the linkage between the Asian summer monsoon and tropopause fold activity over the eastern Mediterranean and the Middle East. J. Geophys. Res. Atmos. 119:3202–3221. https://doi.org/10.1002/2013JD021113
62. Wilcox LJ, Hoskins BJ, Shine KP (2012) A global blended tropopause based on ERA data. Part I: Climatology. Quart. J. Roy. Meteor. Soc. 138:561–575. https://doi.org/10.1002/qj.951
63. World Meteorological Organization (WMO) (1957) World Meteorological Organization. Int. Organ. 11:541–542. https://doi.org/10.1017/S0020818300024127
64. Wu G, Duan A, Liu Y, et al (2015) Tibetan Plateau climate dynamics: recent research progress and outlook. Natl. Sci. Rev. 2:100–116. https://doi.org/10.1093/nsr/nwu045
65. Wu G, Liu Y, Zhang Q, et al (2007) The Influence of Mechanical and Thermal Forcing by the Tibetan Plateau on Asian Climate. J. Hydrometeorol 8:770–789. https://doi.org/10.1175/JHM609.1
66. Wu G, Zhuo H, Wang Z, Liu Y (2016) Two types of summertime heating over the Asian large-scale orography and excitation of potential-vorticity forcing I. Over Tibetan Plateau. Sci. China Earth Sci. 59:1996–2008. https://doi.org/10.1007/s11430-016-5328-2
67. Wu Y, Chen G, Taylor L, Zhang P (2018) On the Linkage Between the Asian Summer Monsoon and Tropopause Folds. J. Geophys. Res. Atmos. 123:2037–2049. https://doi.org/10.1002/2017JD027870

68. Xia Y, Huang Y, Hu Y (2018) On the Climate Impacts of Upper Tropospheric and Lower Stratospheric Ozone. J. Geophys. Res. Atmos. 123:730–739. https://doi.org/10.1002/2017JD027398
69. Xu X, Lu C, Shi X, Gao S (2008) World water tower: An atmospheric perspective. Geophys. Res. Lett. 35:L20815. https://doi.org/10.1029/2008GL035867
70. Xu X, Zhao T, Lu C, et al (2014) An important mechanism sustaining the atmospheric "water tower" over the Tibetan Plateau. Atmos. Chem. Phys. 14:11287–11295. https://doi.org/10.5194/acp-14-11287-2014
71. Yanai M, Wu G (2006) Effects of the Tibetan Plateau. In: Wang B (ed) The Asian Monsoon. Springer, Berlin, Heidelberg, pp 513–549
72. Yang M, Li C, Luo D, et al (2022) Mechanical and Thermal Impacts of the Tibetan–Iranian Plateau on the North Pacific Storm Track: Numerical Experiments by FGOALS-f3-L. J. Geophys. Res. Atmos. 127:e2021JD035659. https://doi.org/10.1029/2021JD035659
73. Yin X, Kang S, de Foy B, et al (2017) Surface ozone at Nam Co in the inland Tibetan Plateau: variation, synthesis comparison and regional representativeness. Atmos. Chem. Phys. 17:11293–11311. https://doi.org/10.5194/acp-17-11293-2017
74. Zeng G, Morgenstern O, Braesicke P, Pyle JA (2010) Impact of stratospheric ozone recovery on tropospheric ozone and its budget. Geophys. Res. Lett. 37:L09805. https://doi.org/10.1029/2010GL042812
75. Zhang Y, Rossow WB, Lacis AA, et al (2004) Calculation of radiative fluxes from the surface to top of atmosphere based on ISCCP and other global data sets: Refinements of the radiative transfer model and the input data. J. Geophys. Res. Atmos. 109:D19105. https://doi.org/10.1029/2003JD004457

Figures

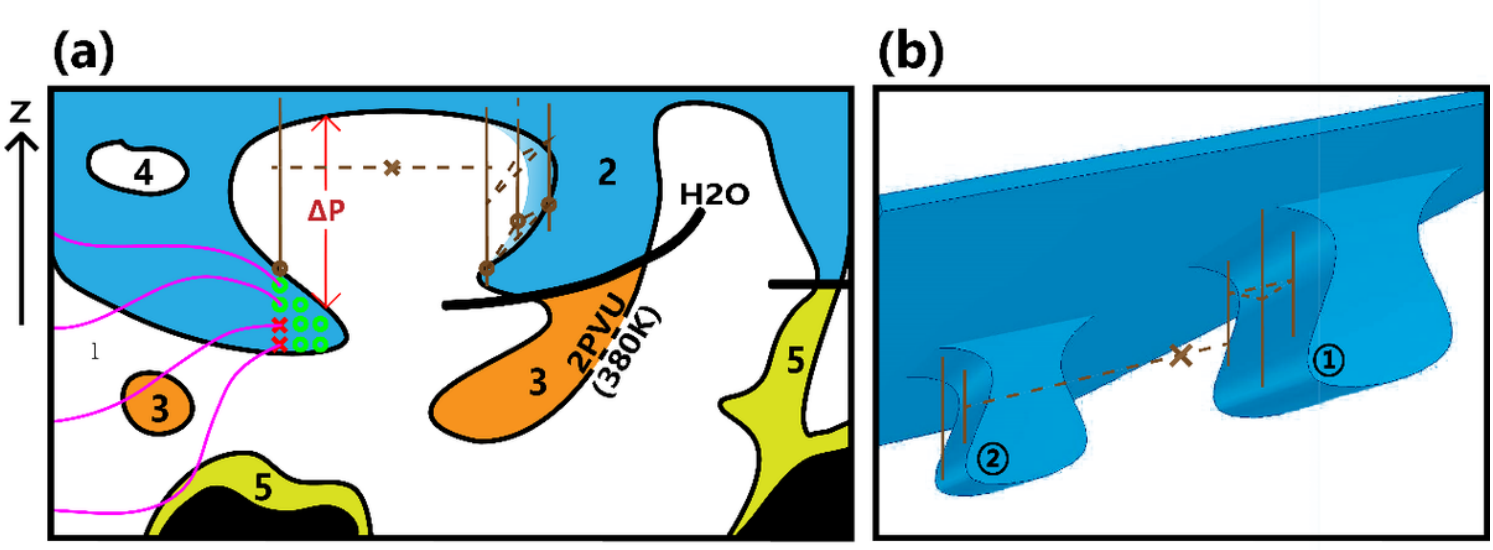

Figure 1

Panel a: Schematic diagram of the improved 3D labeling algorithm. The labels are assigned by the 3D labeling algorithm according to 2 PVU surfaces (thin black line) (or θ = 380 K) as follows (a, taken from Škerlak et al., (2015), their Figure 1): label 1 for tropospheric air, label 2 for stratospheric air, label 3 for isolated stratospheric air or cyclonic PV anomalies formed by diabatic processes (stratospheric cutoffs), label 4 for isolated tropospheric air (tropospheric cutoffs), label 5 for cyclonic PV anomalies generated by surface friction. Black shadings represent orography and thick black lines indicate cutoffs. Label 2 and 3 are separated according to the specific humidity (threshold 0.1 $g \cdot kg^{-1}$). If frictionally formed PV anomalies are connected to the stratospheric PV anomalies, such as label 2 and 5, they are separated in height with minimal horizonal cross sections. The pressure difference ΔP is used to classify the tropopause fold. Finally, a Lagrangian filter is applied for the grid points inside the fold to further exclude the air mass with PV anomalies formed by diabatic and frictional processes. The solid pink lines indicate the path traced by the backward trajectory, the green circles stand for the air that passes the Lagrangian filter (intruded air from the stratosphere) and the red cross for the air that does not (diabetically and frictionally generated PV anomalies). Panel b: Improvement of connectedness with and representing folding events, solid brown lines for pressure differences, dashed lines for connectedness detection and brown crosses for failure connections.

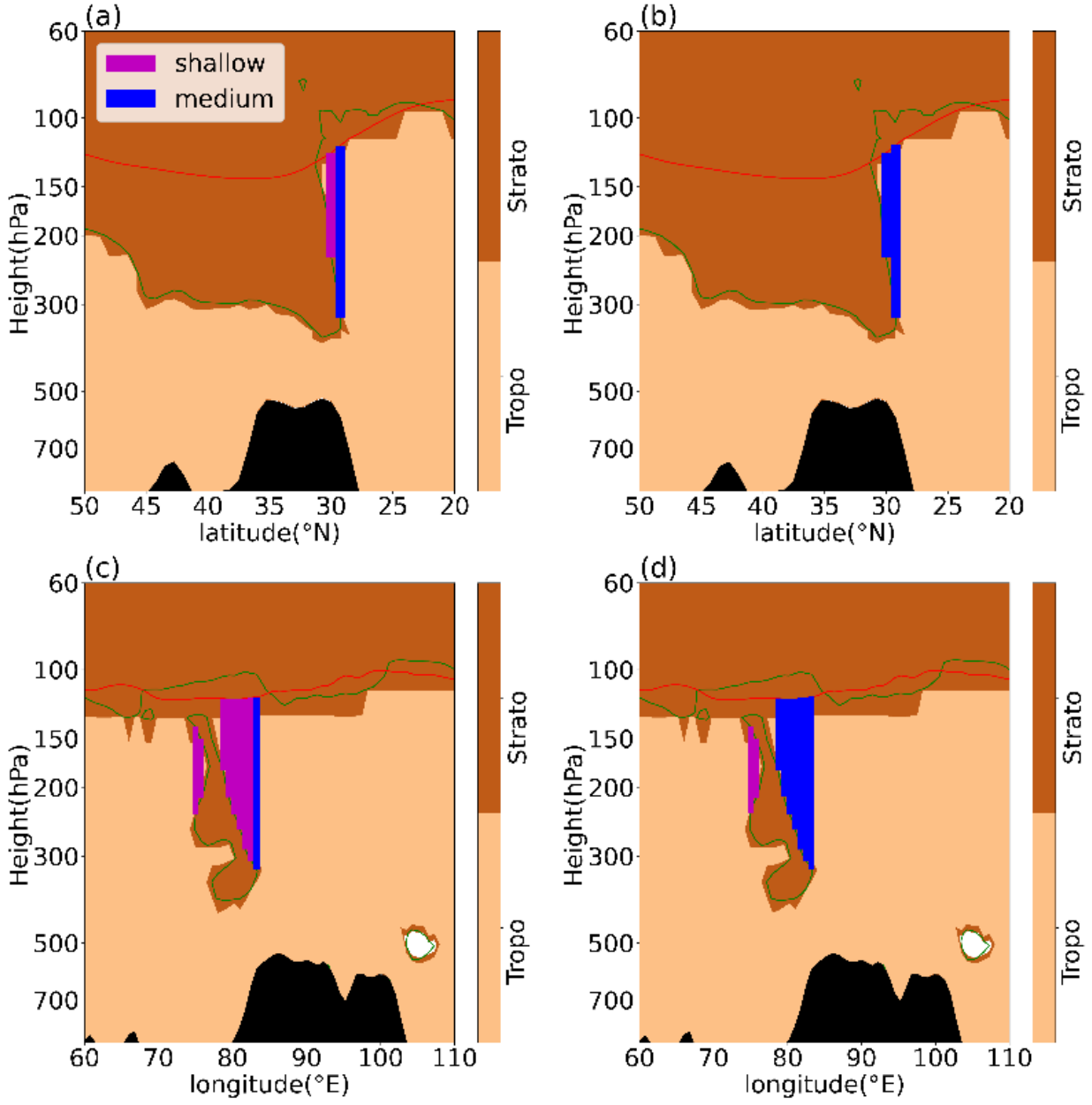

Figure 2

Vertical distribution of a tropopause fold over the TP as detected by the 3D labeling algorithm before (a and c) and after (b and d) algorithm improvement on February 25, 2008 at 06 UTC (a and b are aligned along 83.25°E from 50°N to 20°N, c and d along 29.25°N from 60°E to 110°E). Purple and blue shading represent shallow ($50 \leq \Delta P < 200$ hPa) and medium ($200 \leq \Delta P < 350$ hPa) folds respectively. The red line indicates the 2 PVU isosurface. The green line indicates the 380 K isosurface. The black area represents

the topography and white shading represent PV anomalies. Filled color indicates tropospheric (light brown) and stratospheric air (dark brown) as identified by the 3D labeling algorithm.

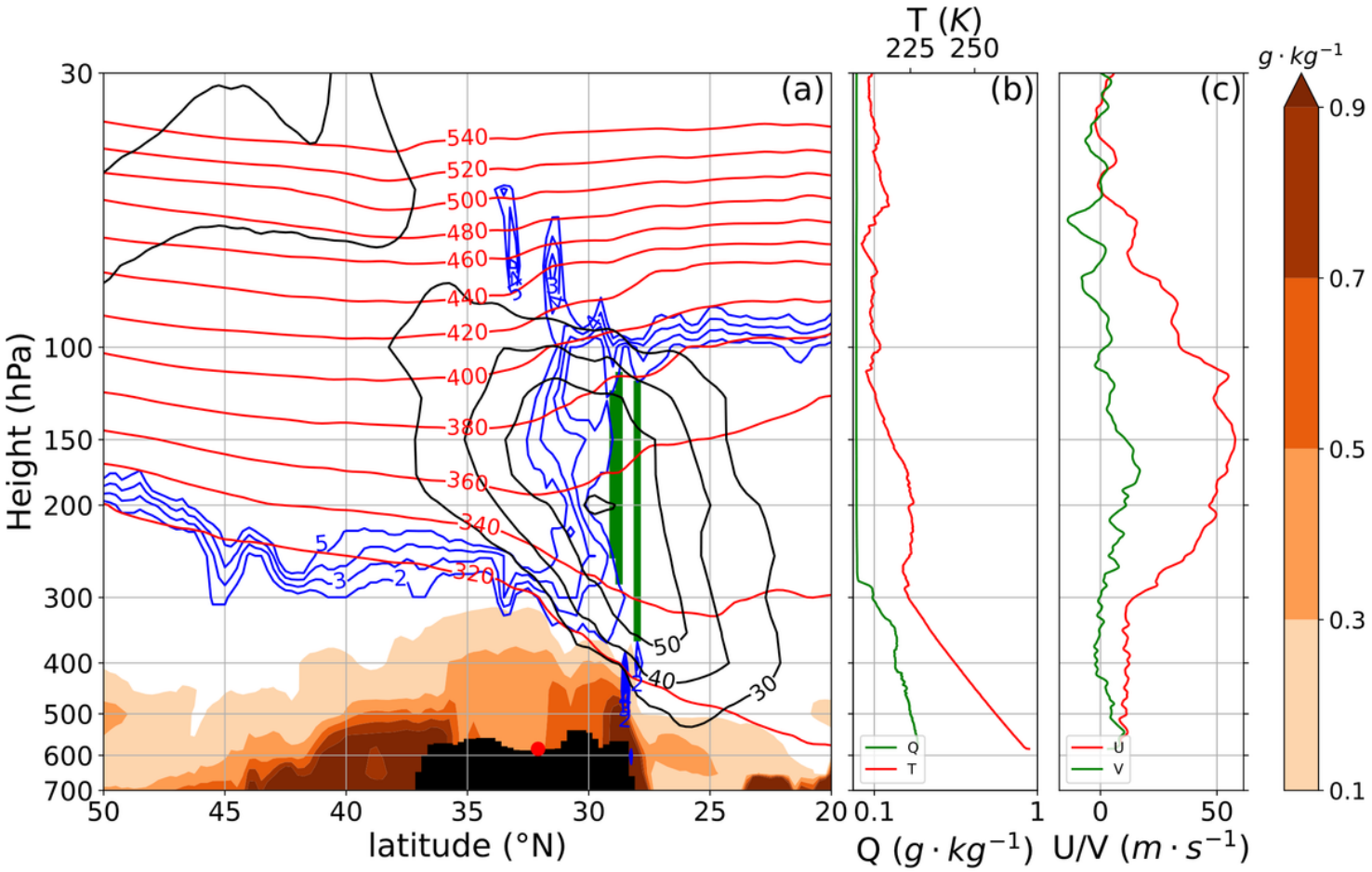

Figure 3

Latitudinal section of the tropopause fold (green shading: area between the first tropopause and the second tropopause) over the TP at 11 UTC on February 25, 2008 (84.25 °E). (a) Isentropic (in K, red contours), potential vorticity values of 2~5 PVU, and zonal wind speed ($m \cdot s^{-1}$, black contours); (b) specific humidity, temperature; and (c) wind speed components of the GPS sounding profiles.

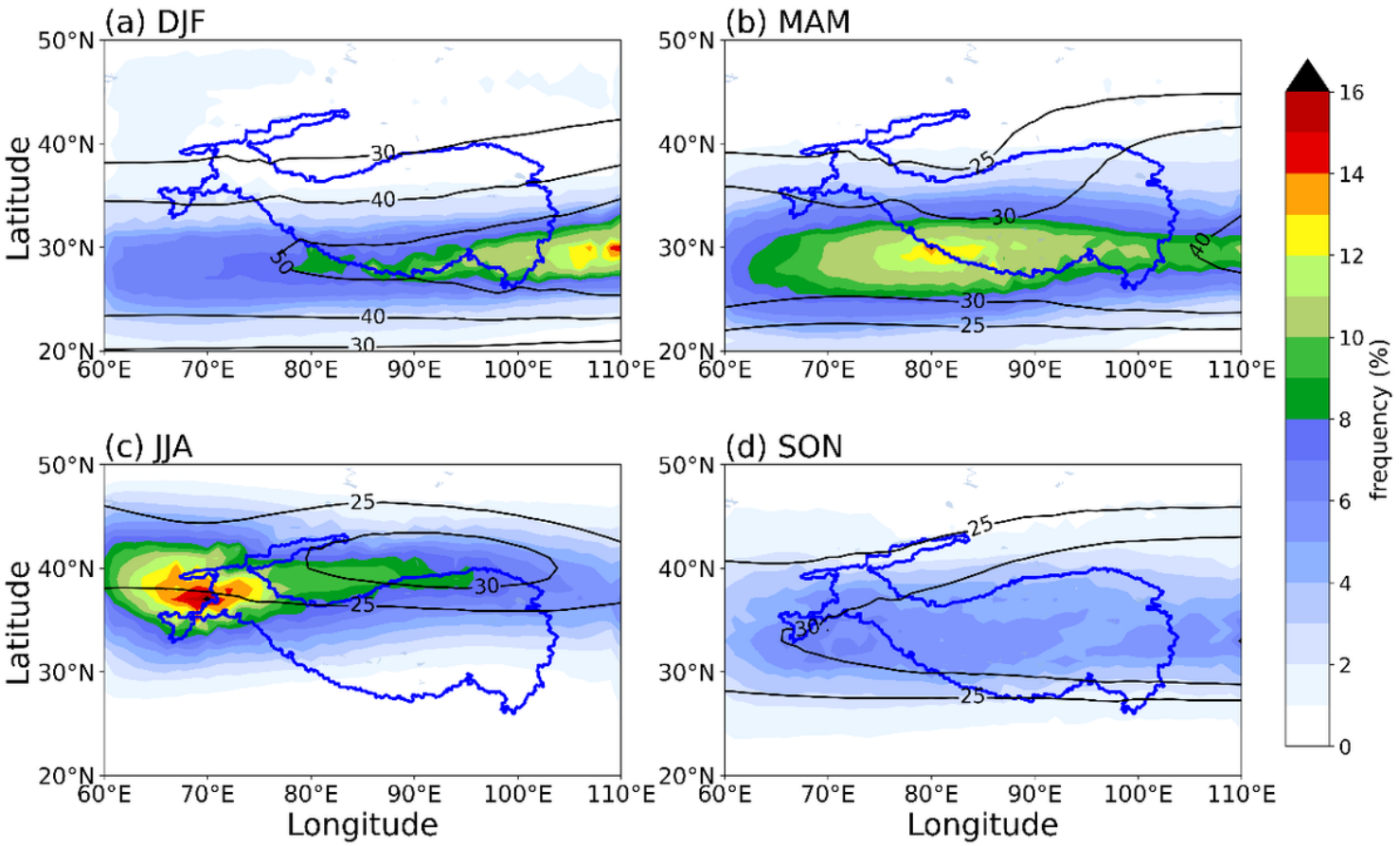

Figure 4

Seasonal averages of the tropopause fold frequencies identified by the improved 3D labeling algorithm in (a) December, January, and February (DJF), (b) March, April and May (MAM), (c) June, July and August (JJA), and (d) September, October and November (SON) over the Tibetan Plateau during 1979-2019. The black contours are the zonal wind at 200 hPa ($m \cdot s^{-1}$). The Tibetan Plateau is delineated by blue contour lines (3 km elevation).

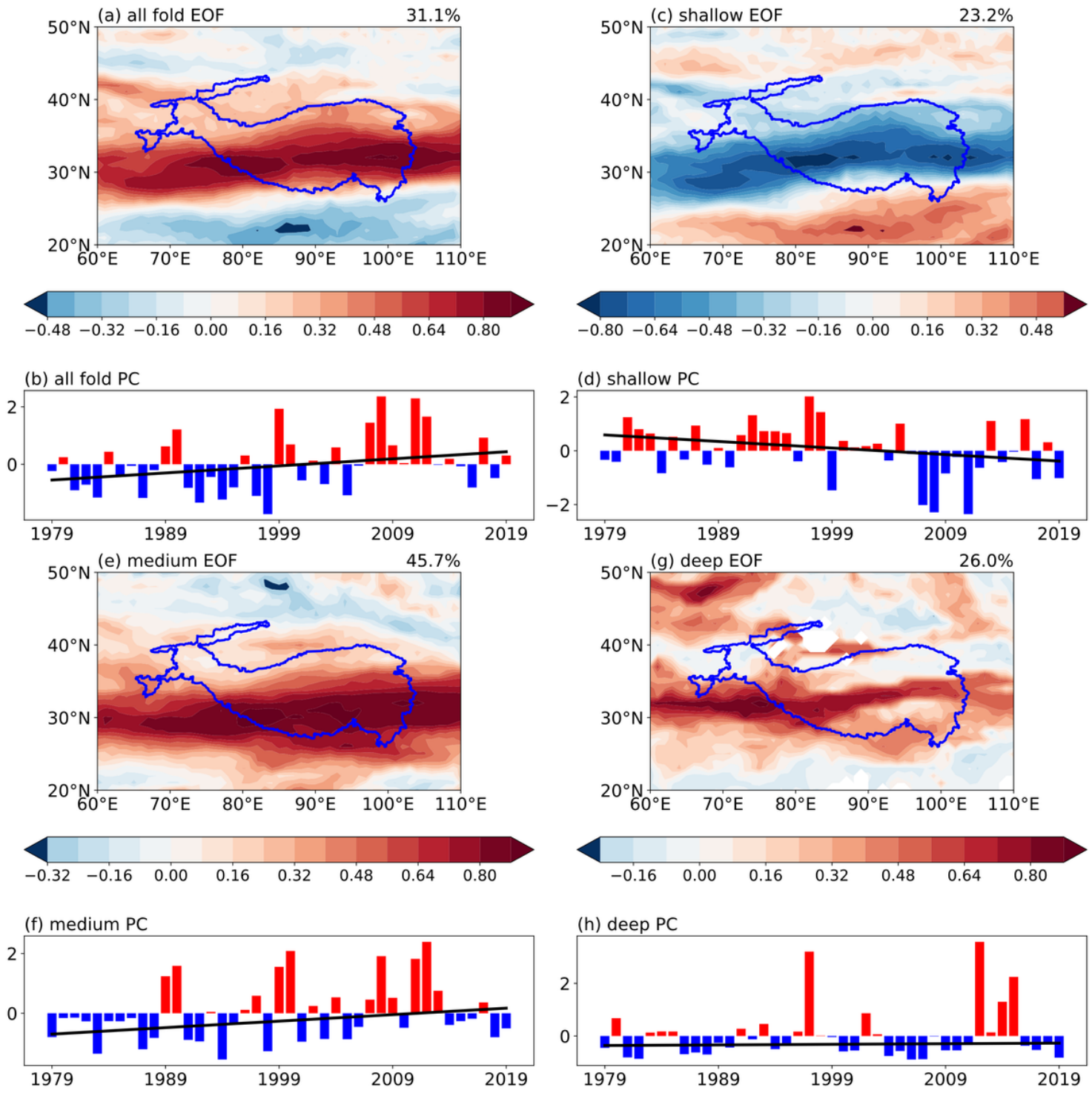

Figure 5

Spatial patterns and temporal amplitudes of the first EOF modes of tropopause fold frequencies over the TP during 1979-2019. First EOF modes of total folds (a), shallow folds (c), medium folds (e), and deep folds (g), respectively. Time series of the first EOF of total folds (b), shallow folds (d), medium folds (f), and deep folds (h) with trend (black lines, at a 95% confidence level). Explained variances of the first EOF patterns of the fold frequencies are listed on the right corner of each panel.

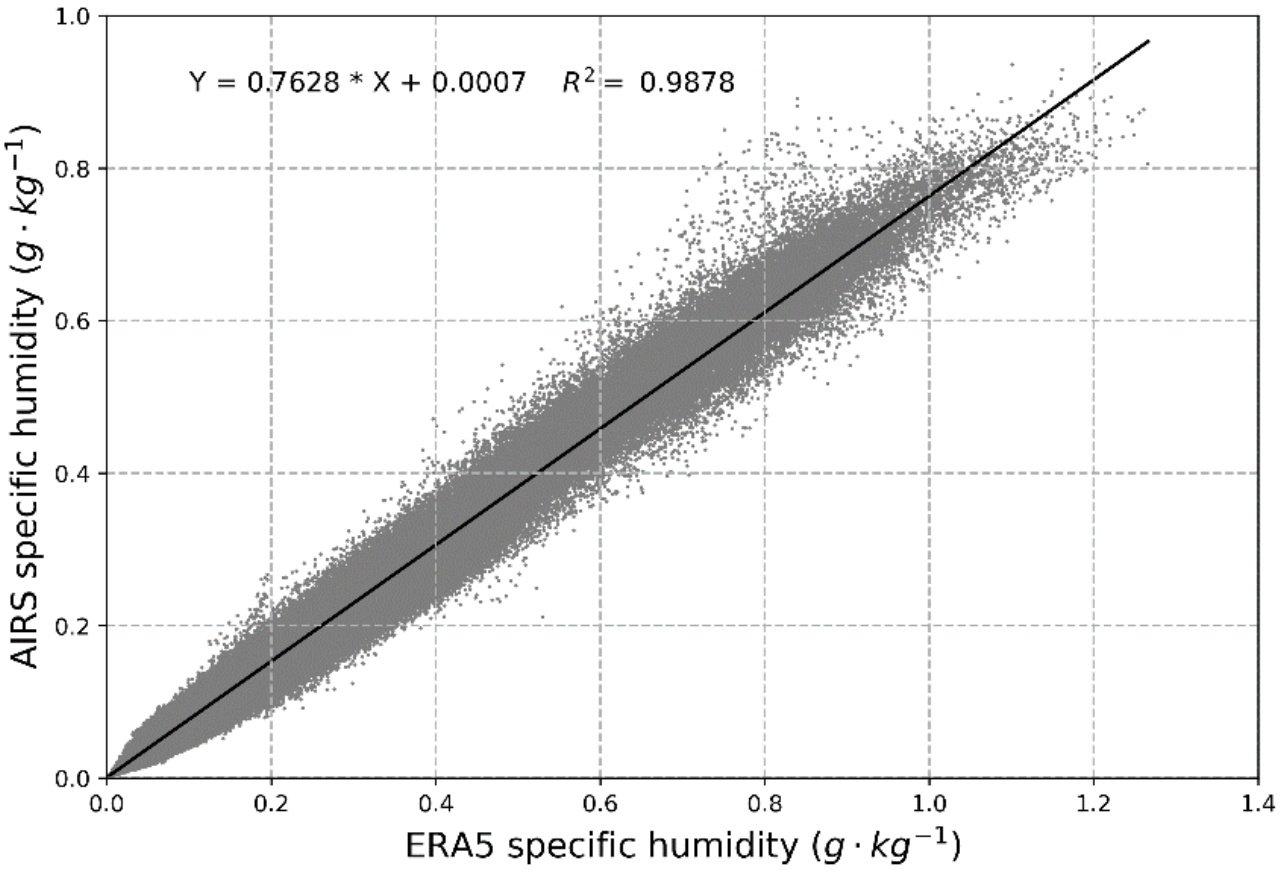

Figure 6

Scatter plot of specific humidity of the ERA5 reanalysis data and the AIRS at the same grid point and the same time. Ranges are 20.5-49.5°N, 60.5-109.5°E, and height is 300 hPa-100 hPa. The solid line represents the regression, and the regression equation and R^2 are also shown in the upper left corner.

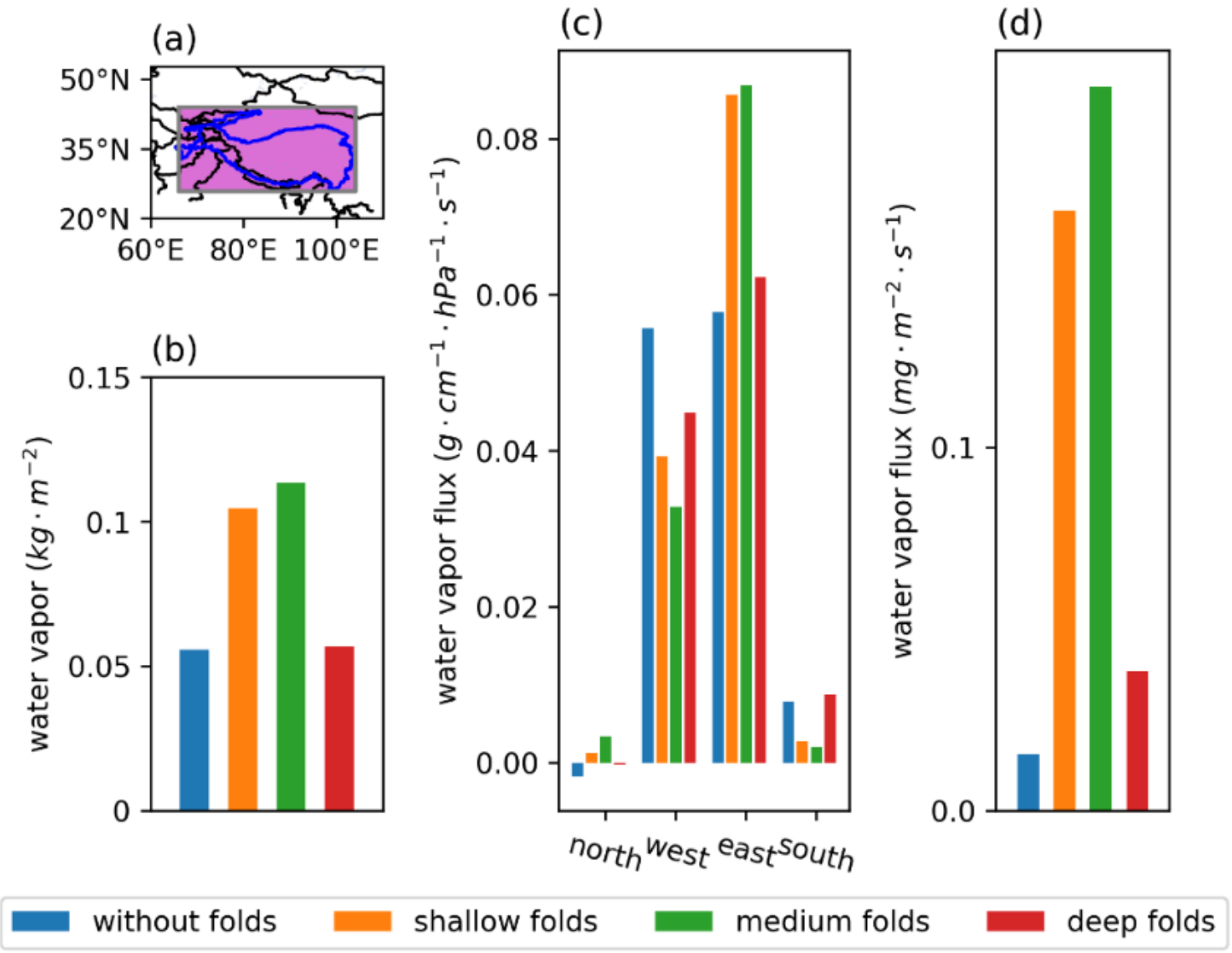

Figure 7

(b) Water vapor content ($kg \cdot m^{-2}$), (c) Average water vapor flux ($g \bullet cm^{-1} \bullet hPa^{-1} \bullet s^{-1}$) at the north, west, east and south boundaries and (d) mean vertical water vapor flux ($mg \bullet m^{-2} \bullet s^{-1}$) in the UTLS (300-50 hPa) over the TP (shaded area in a) for no fold and different classes of folds. Blue is for no fold, orange for shallow folds, green for medium folds, and red for deep folds.

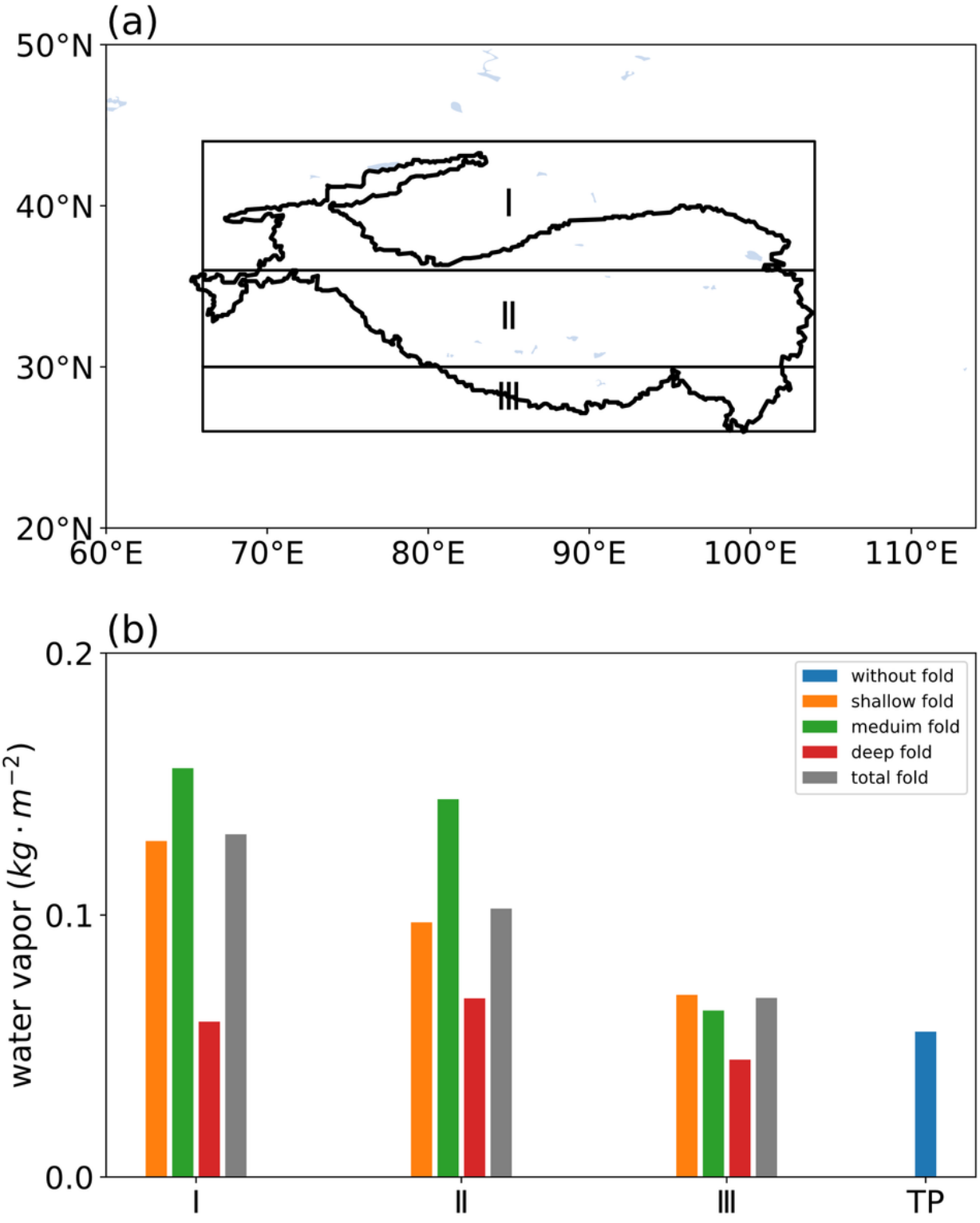

Figure 8

Average amount of water vapor in a column of UTLS (kg•m^{-2}) corresponding to folds in different regions of the Tibetan Plateau from 1979 to 2019. (a) Regions I (44°N-36°N), II (36°N-30°N) and III (30°N-26°N) represent the northern, central, and southern TP, respectively. (b) Gray, orange, green, red and blue represent UTLS water vapor of total folds, shallow folds, medium folds, deep folds, and no folds, respectively.

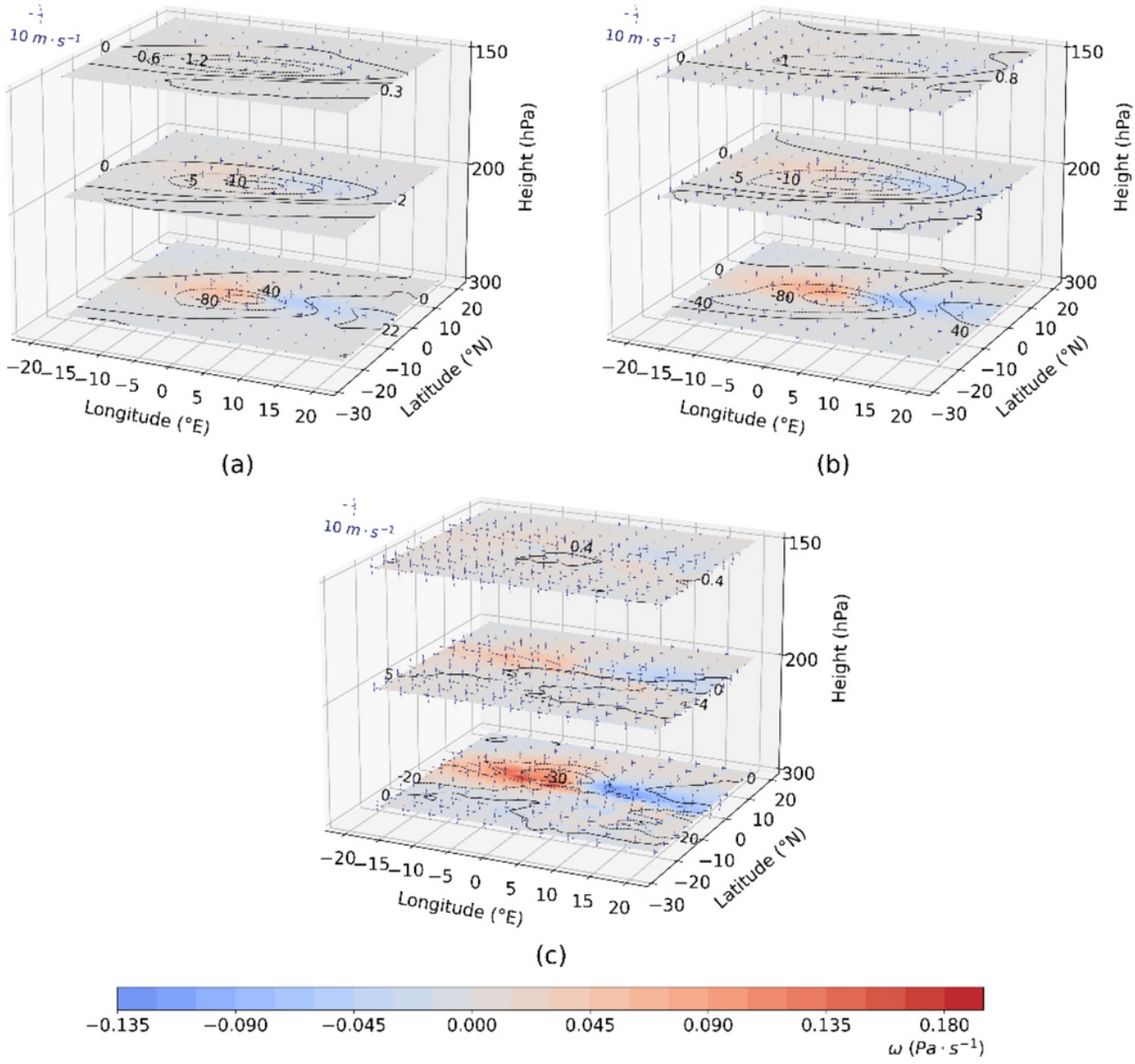

Figure 9

Distributions of vertical velocity anomalies (colored), water vapor mixing ratio anomalies (contours, ppmv) and wind vector anomalies (arrows) at the pressure levels of 150 hPa, 200 hPa, and 300 hPa in UTLS of the Tibetan Plateau during 1979-2019. The latitude and longitude of the grid points correspond to the deepest points of the fold (0°N, 0°E) in (a) shallow, (b) medium and (c) deep folds.

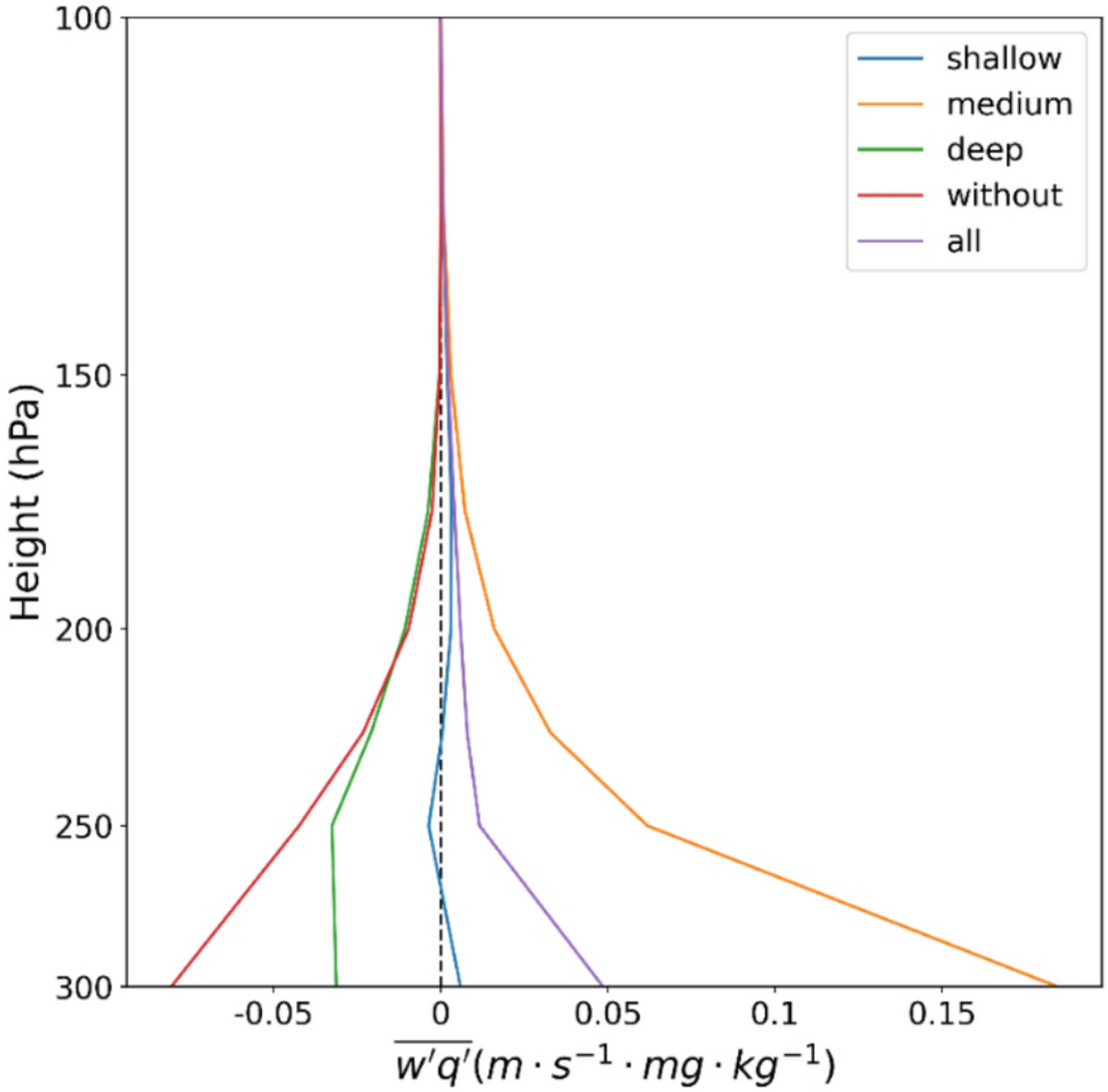

Figure 10

Vertical profiles of the subgrid perturbed water vapor flux in the UTLS over the TP during 1979-2019. The blue, orange, green, red and purple line represents the shallow, medium, deep fold, no fold and all fold, respectively.

Supplementary Files

This is a list of supplementary files associated with this preprint. Click to download.

- supportinformation.pdf